Nuclear Engineering and Design 415 (2023) 112744

Contents lists available at ScienceDirect

Nuclear Engineering and Design

journal homepage: www.elsevier.com/locate/nucengdes

# Eccentric drop of a control rod in the guide tube with annular gap flow

Jun Liu [a,b,1], Luyao He [c,1], Qing Peng [a,b], Xiaodong Chen [d], Xiaoming Liu [a,b,*], Yueguang Wei [e]

[a] LNM, Institute of Mechanics, Chinese Academy of Sciences, Beijing 100190, PR China
[b] School of Engineering Science, University of Chinese Academy of Sciences, Beijing 100049, PR China
[c] School of Medical Technology, Beijing Institute of Technology, Beijing 100081, PR China
[d] School of Aerospace Engineering, Beijing Institute of Technology, Beijing 100081, PR China
[e] College of Engineering, Peking University, Beijing 100871, PR China

ARTICLE INFO

*Keywords:*
Control rod drop
Annular gap flow
Eccentricity effect
Added mass
Hydrodynamic characteristics
Dynamic mesh technique

ABSTRACT

The drop time of control rod is essential for safety analysis of nuclear power plant. The motion of control rod can be characterized by an annular gap flow with large blockage ratio. In this study, we studied the effects of the eccentricity between the control rod and the guide tube on the annular gap flow, and further on the drop time. By considering the added mass and the upward flow of fluid in the annular gap, we developed a theoretical model for computing the drop time of eccentric rod. In the proposed model, particularly, the annular gap flow velocity was obtained from full-scale computational fluid simulations with respect to blockage ratio and eccentricity. The simulation and experiment results agree well on the drop time, the histories of velocity and acceleration, and the hydrodynamic characteristics. Results show that the drop time increases drastically when blockage ratio $\alpha$ increases from 0.83 to 0.91, and the eccentricity effect on drop time is negligible when the blockage ratio is small (e.g., $\alpha < 0.83$). Nevertheless, for large blockage ratio ($\alpha \geq 0.83$), the drop time increases significantly for eccentric rod drop, especially for a lighter control rod. The present study provides a general method for analysis of control rod drop, which is critical for the nuclear reactor design.

## 1. Introduction

In the nuclear reactor, the control rod can quickly control the absorption of neutron to achieve reactor startup, power regulation, power maintenance, and safe shutdown under normal and accident conditions (Yoon et al., 2009). Dropping in a guide tube with annular gap flow (Andriambololona et al., 2007), the control rod drive mechanism (CRDM) is required to move slowly to ensure the safety of the reactor under normal working conditions; while in the accident condition (e.g., seismic or loss of coolant), the CRDM has to be quickly inserted into the core to protect the reactor (Wang et al., 2003; Huang et al., 2018; Cheng et al., 2020). Therefore, drop time is one crucial parameter for the design of the CRDM. It should be mentioned that if the drop time of the CRDM is considered without other matters, it is generally expected to be as short as possible (Cheng et al., 2020). However, the reduction of drop time will lead to a higher speed and a great impact on the fuel assembly, a buffer spring can display a buffer role when the CRDM is about to approach the bottom of the guide tube.

Numerous researches have studied the dynamics of CRDM on various accident conditions theoretically, experimentally and numerically. In an early study by Donis and Goller (1972), a mathematical model for the single control rod was proposed for the accident analysis in a pressurized water reactor (PWR, Generation-II), however this work neglected the added mass effect, and the hydraulic drag coefficient is uncertain. In another study, Taliyan et al. (1994) presented a theoretical model of the shut-off rod drop in a Pressurized Heavy Water Reactor (PHWR, Generation-II) and verified experimentally. Based on fluid mechanics and boundary layer theory, Yu et al. (2001) discussed the effect of fluid viscous drag and pressure drag during the drop process. With the steady development of new nuclear reactors, using a sodium cooled fast reactor (SFR, Generation-IV) as the research object, Rajan Babu et al. (2014) presented the salient features of the safety rod and its mechanism, further, the sensitivity analysis of parameters was also conducted. Lin et al. (2017) proposed a model for the control rod drop in a thorium-based molten salt reactor (TMSR, Generation-IV) and verified that the drop time in the molten salt is satisfied with the limiting drop time. Recently, Arthur et al. (2020) carried out a control rod drop analysis for a lead-based fast reactor (LFR, Generation-IV) with a high-power density and high boiling point, they obtained the nonlinear differential

* Corresponding author at: LNM, Institute of Mechanics, Chinese Academy of Sciences, Beijing 100190, PR China.
*E-mail address:* xiaomingliu@imech.ac.cn (X. Liu).
[1] Jun Liu and Luyao He contributed equally to this work.

https://doi.org/10.1016/j.nucengdes.2023.112744
Received 26 July 2023; Received in revised form 29 October 2023; Accepted 3 November 2023
Available online 15 November 2023

**Nomenclature**

| | |
|---|---|
| $a$ | accelerations of control rod drop |
| $A_{rea}$ | cross-sectional area of control rod |
| $c(x, t)$ | volume fraction field |
| $C_D$ | drag coefficient |
| $C_i$ | laminar flow geometric parameters for non-circular pipes |
| $C_{i0}$ | laminar flow geometric parameters for circular pipes |
| $C_t$ | turbulent geometric parameter for non-circular pipes |
| $C_{t0}$ | turbulent geometric parameter of a circular pipe |
| $D_E$ | equivalent diameter of annular channel |
| $f$ | dimensionless viscous friction coefficient |
| $\boldsymbol{f}_\sigma$ | surface tension force |
| $F$ | sum of the buoyancy, fluid inertia force, viscous friction drag, and pressure drag |
| $\boldsymbol{F}$ | source term for the momentum equation |
| $F_a$ | inertial force of the fluid |
| $F_B$ | buoyant force acting on the control rod |
| $F_f$ | viscous frictional frag |
| $F_p$ | pressure drag |
| $g$ | gravitational acceleration |
| $G$ | gravity of the control rod |
| $k$ | added mass coefficient |
| $l$ | contact length between control rod and fluid |
| $L$ | length of the control rod |
| $m$ | total mass of the control rod |
| $m'$ | the added mass |
| $r$ | outer diameter of the control rod |
| $R$ | inner diameter of the guide tube |
| $Re$ | Reynolds number |
| $S_\phi$ | the source term of $\phi$ |
| $t$ | drop time |
| $\boldsymbol{u}$ | velocity vector |
| $\boldsymbol{u}_g$ | speed of grid motion |
| $v$ | relative velocity between the control rod and the fluid flow |
| $v_w$ | upward annular gap flow velocity of fluid |
| $V_a$ | average flow velocity of the cross-section of the annular gap |
| $V_B$ | volume of control rod immersed in fluid |
| $y$ | control rod drop displacement |

*Greek symbols*

| | |
|---|---|
| $\alpha$ | ratio of the outer diameter of the control rod to the inner diameter of the guide tube |
| $\beta$ | nondimensional eccentricity |
| $\gamma$ | correction coefficient for annular gap flow velocity |
| $\delta$ | absolute eccentricity between the control rod and the guide tube |
| $\mu$ | dynamic viscosity |
| $\mu_1$ | dynamic viscosity of water |
| $\mu_2$ | dynamic viscosity of air |
| $\nu$ | kinematic viscosity of fluid |
| $\rho$ | density of the fluid |
| $\rho_1$ | density of water |
| $\rho_2$ | density of air |
| $\phi$ | general scalar quantity |
| $\Gamma$ | diffusion coefficient |

*Acronyms*

| | |
|---|---|
| CFD | computational fluid dynamics |
| CRDM | control rod drive mechanism |
| FBR | Fast Breeder Reactor |
| FSI | fluid-structure interaction |
| FVM | finite volume method |
| INET | Institute of Nuclear Energy Technology |
| LBE | Lead Bismuth Eutectic |
| LCTR | Large Component Test Rig |
| LFR | lead-based fast reactor |
| NHR | nuclear heating reactor |
| PGSFR | prototype generation IV sodium-cooled fast reactor |
| PHWR | Pressurized Heavy Water Reactor |
| PWR | pressurized water reactor |
| SFR | sodium cooled fast reactor |
| SIMPLE | Semi-Implicit Method for Pressure Linked Equations |
| TMSR | thorium-based molten salt reactor |
| TV | Test Vessel |
| VOF | volume of fluid |

equations of the control rod drop and Lead Bismuth Eutectic (LBE) flow, then the influence of physical parameters on rod drop time was investigated.

In experimental studies, Bo et al. (2000), Bo et al. (2002) developed a hydraulic CRDM for the nuclear heating reactor (NHR-200) and demonstrate its performance experimentally on an experimental loop in Institute of Nuclear Energy Technology (INET) of Tsinghua University. Subsequently, the full-scale assembly of prototype control rod of Fast Breeder Reactor (FBR) construction at Kalpakkam, India has been tested in Test Vessel-1 (TV-1) of Large Component Test Rig (LCTR) in air, argon and in sodium for their fail-safe operation by Rajan Babu et al. (2010). In Korea, the prototype generation IV sodium-cooled fast reactor (PGSFR), for which construction is projected to occur by 2028, has been under development since 2012 according to a long-term plan; the drop performance tests of the conceptually designed control rod and the modified control rod are currently being conducted by Kim et al. (2016), Lee et al. (2017) and Son et al. (2019).

Additionally, several studies have been done to study the drop of the control rod using the computational fluid dynamics (CFD) approach (Yoon et al., 2009; Singh et al., 2014; Rabiee and Atf, 2016; Huang et al., 2018; Cheng et al., 2020). Yoon et al. (2009) studied the fluid–structure interaction (FSI) during a PWR control rod drop by finite element analysis. Rabiee and Atf (2016) simulated the unsteady flow field around the control rod inside the guide tube in the control rod drop accident with layering dynamic mesh strategy for a PWR. Cheng et al. (2020) established a three-dimensional numerical simulation of the control rod in a low-temperature heating reactor using dynamic meshing technology and the behavior of dropping the control rod was obtained.

The above investigations all focused on the drop of a concentrically located control rod. However, eccentricity of the control rod positioned in the guide tube is inevitable due to the manufacturing and assembling errors, structural deformations (Mateescu et al., 1994), etc. The presence of eccentricity in annular configurations adds considerably to the complexity of the problem and has been only scarcely investigated. Thus, in the present study, we aimed at exploring the eccentricity effect on control rod drop.

In this study, we proposed a theoretical model for the drop time of eccentric rod considering added mass and the annular gap flow of fluid. The upward annular gap flow velocity under large blockage ratio and large eccentricity is determined by full-scale simulations. For validation, we designed an experimental device to realize the annular gap flow during the eccentric rod drop. Finally, we investigated analytically the eccentricity effect on the control rod drop time, velocity, acceleration, and the hydrodynamic characteristics.

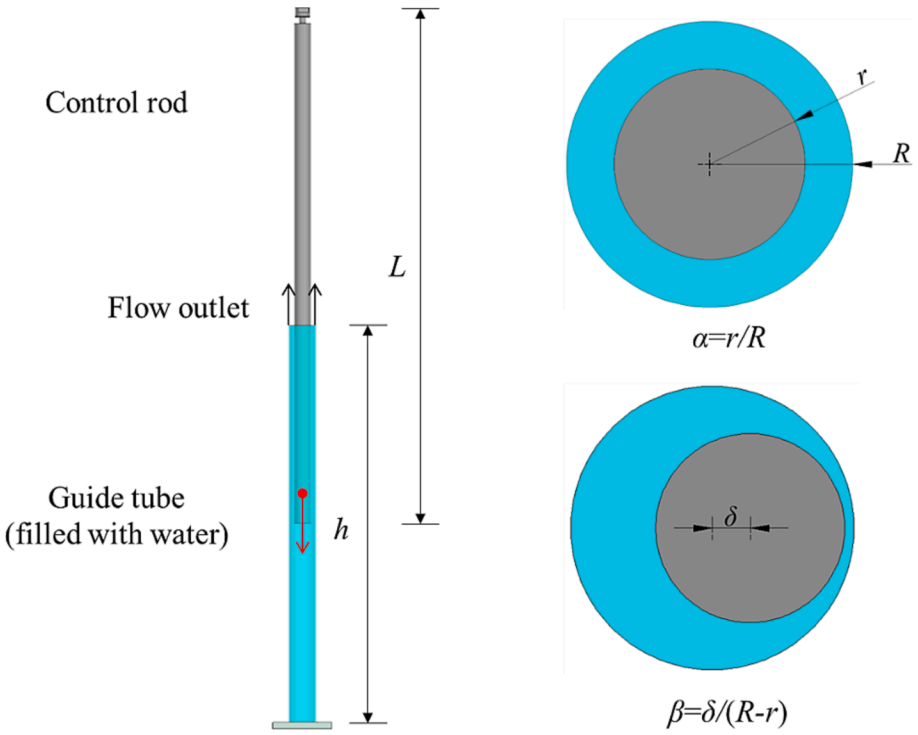


**Fig. 1.** Schematic diagram of eccentric rod drop. The area shaded with green color represents the fluid domain.

## 2. Theoretical model of eccentric rod drop

In different cases of control rod, the CRDM has various forms of flow channels. In this study, we mainly focused on the rod drop state of water reactor control rods, and a single channel was considered. The single channel means that the fluid has only one flow channel, which is the annular channel of control rod and guide tube (Zhao et al., 2022). With the drop of the control rod, a portion of the fluid flows upwards through the annular gap, forming a gap jet flow.

Fig. 1 shows a schematic of the eccentric rod drop. The blockage ratio, $\alpha$, is defined as the ratio of the outer diameter of the control rod ($r$) to the inner diameter of the guide tube ($R$), i.e., $\alpha = r/R$. The absolute eccentricity between the control rod and the guide tube is denoted with $\delta$. The non-dimensional eccentricity, $\beta$, is defined as the ratio of the absolute eccentricity ($\delta$) to the diameter difference of guide tube and control rod ($R$-$r$), i.e., $\beta = \delta/(R\text{-}r)$. When $\delta$ or $\beta$ is equal to zero, the problem is corresponding to concentric rod drop.

### 2.1. Governing equation of eccentric rod drop

When the control rod drops in a viscous fluid, the forces acting on the control rod are gravity, buoyancy, fluid forces caused by added mass, viscous friction drag, and pressure drag. The motion of the control rod is thus governed by the equation of motion:

$$G - F_B - F_a - F_f - F_p = m\frac{d^2y}{dt^2} \tag{1}$$

in which $G$ is the gravity of the control rod, $F_B$ is the buoyant force acting on the control rod, $F_a$ is the inertial force of the fluid, $F_f$ is the viscous frictional frag, $F_p$ is the pressure drag, $m$ is the total mass of the control rod, $y$ is the control rod drop displacement, and $t$ is the drop time.

### 2.2. Force analysis

(1) Gravity

Gravity is the force exerted on the control rod by the attraction of the earth, which is proportional to the acceleration of gravity, i.e.

$$G = mg \tag{2}$$

in which $g$ is the gravitational acceleration.

(2) Buoyancy

Buoyancy is caused by the difference in hydrostatic pressure on the surface of an object immersed in a fluid:

$$F_B = \rho V_B g \tag{3}$$

in which $\rho$ is the density of the fluid ($\rho \approx 998$ kg/m$^3$ for the water at 20℃), $V_B$ is the volume of control rod immersed in fluid and can be calculated as follows:

$$V_B = yA_{rea} \tag{4}$$

in which $A_{rea}$ is the cross-sectional area of control rod, i.e., $A_{rea} = \pi r^2$.

(3) Fluid inertia force

When the control rod drops in an unsteady state in the fluid, the inertial force exerted by the fluid on the control rod is equivalent to the inertial force generated by a mass attached to the mass of the control rod (Chen, 1975), i.e.

$$F_a = m'\frac{d^2y}{dt^2} \tag{5}$$

in which $m'$ is the added mass. It should be noted that the direction of the inertial force of the fluid is opposite to the direction of the control rod's acceleration. The added mass can usually be expressed in the following form (Chen, 1975):

$$m' = k\rho V_B \tag{6}$$

in which $k$ is the added mass coefficient. The added mass coefficient is

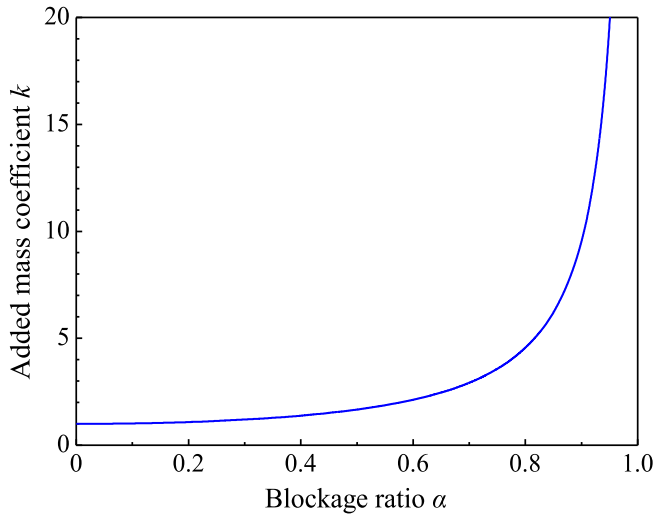


**Fig. 2.** Added mass coefficient as function of blockage ratio for concentrically located control rod.

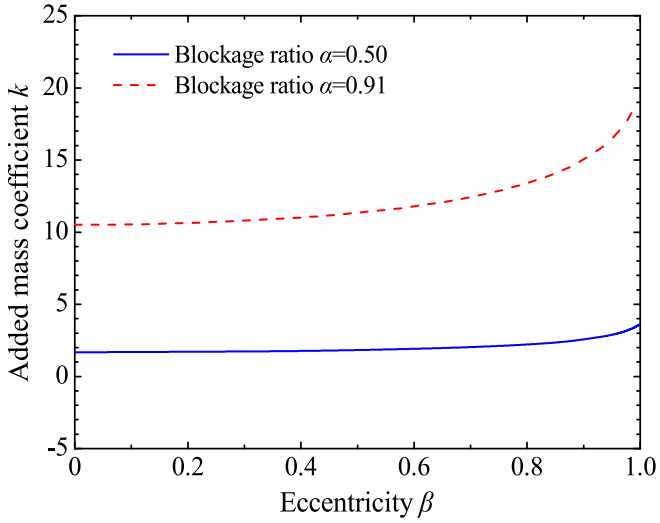


**Fig. 3.** Added mass coefficient as function of eccentricity for blockage ratio $\alpha$ = 0.50 and 0.91.

**Table 1**
Theoretical calculation conditions.

| | $\beta = 0$ | $\beta = 1.0$ |
|---|---|---|
| $\alpha = 0.50$ ($r = 50$ mm, $R = 100$ mm) | Case 1 | Case 2 |
| $\alpha = 0.67$ ($r = 50$ mm, $R = 75$ mm) | Case 3 | Case 4 |
| $\alpha = 0.83$ ($r = 50$ mm, $R = 60$ mm) | Case 5 | Case 6 |
| $\alpha = 0.91$ ($r = 50$ mm, $R = 55$ mm) | Case 7 | Case 8 |

generally taken as 1.0 for infinite domain fluids. But for an annular gap flow with outer diameter $R$ and inner diameter $r$, the added mass coefficient $k$ is related to blockage ratio $\alpha$. Based on the two-dimensional potential flow theory, Chung and Chen (1977) presented an analytical method for evaluating the hydrodynamic masses of a group of circular cylinders immersed in a fluid contained in a cylinder. For a concentrically located control rod, the added mass can be calculated by the following formula (Yu et al., 2001):

$$k = \frac{R^2 + r^2}{R^2 - r^2} = \frac{1 + \alpha^2}{1 - \alpha^2} \tag{7}$$

When $R \gg r$, the blockage ratio $\alpha$ is approaching to zero, which corresponds to an infinite domain fluid, and thus $k = 1.0$. It can also be seen from Eq. (7) that the added mass coefficient increases with the increase of blockage ratio. Fig. 2 gives the variation of added mass coefficient with blockage ratio for a concentrically located control rod.

The added mass coefficient $k$ is also related to the eccentricity $\beta$ for an eccentrically positioned control rod. Fig. 3 shows the variations of added mass coefficient with eccentricity for two values of blockage ratio $\alpha$ equals to 0.50 and 0.91 (Chung and Chen, 1977), respectively. As indicated by Fig. 3, the added mass coefficient increases with the increase of eccentricity, and the added mass coefficient at the eccentricity of 1.0 is about twice that of at the center alignment state. For eccentricity $\beta > 0.91$, Gibert (1988) gave an explicit expression of added mass coefficient $k$.

(4) Viscous friction drag

The wall viscous friction drag of control rod in annular channel is caused by the boundary layer effect of viscous fluid, i.e., the shear stress acting on the wetted surface. Usually, when calculating the friction drag in an annular channel, the friction drag formula in the circular tube can be adopted, but the equivalent diameter of the annular channel is used to replace the diameter of the circular tube in the friction resistance calculation formula (Zhou et al., 2013; Rajan Babu et al., 2014). Thus, the viscous friction drag acting on the control rod can be calculated with (Zhou et al., 2013):

$$F_f = f \frac{l}{D_E} \frac{1}{2} \rho v^2 A_{rea} \tag{8}$$

in which $f$ is the dimensionless viscous friction coefficient; $l$ is the contact length between control rod and fluid, it is equal to the control rod drop displacement $y$ in this study; $D_E$ is the equivalent diameter of annular channel; $v$ is the relative velocity between the control rod and the fluid flow.

The equivalent diameter $D_E$ can be calculated by the following formula:

$$D_E = R - r \tag{9}$$

The dimensionless viscous friction coefficient $f$ is related to parameters such as Reynolds number and wall roughness. For laminar flow, $f$ can be calculated by the following formula:

$$f = \frac{64}{Re} \tag{10}$$

and for turbulent flow, $f$ can be calculated with (Wang et al., 1994):

$$f = C_t Re^{-0.25} \tag{11}$$

$$C_t / C_{t0} = \sqrt[3]{0.0154 \frac{C_i}{C_{i0}} - 0.012} + 0.85 \tag{12}$$

in which $C_{t0}$ is the turbulent geometric parameter of a circular pipe, $C_{t0} = 0.3164$ in hydraulically smooth areas; $C_t$ is the turbulent geometric parameter for non-circular pipes; $C_i$ and $C_{i0}$ are laminar flow geometric parameters for non-circular and circular pipes, respectively. In this study, $C_t$ can be taken as 0.3395 according to the size ratio of the actual control rod drive line.

$Re$ is the Reynolds number and defined as follows:

$$Re = \frac{v D_E}{\nu} \tag{13}$$

in which $\nu$ is the kinematic viscosity of fluid ($\nu \approx 1.003 \times 10^{-6}$ m$^2$/s for the water at 20℃).

The relative velocity $v$ between the control rod and the fluid is the velocity at which the control rod drops plus the velocity at which the

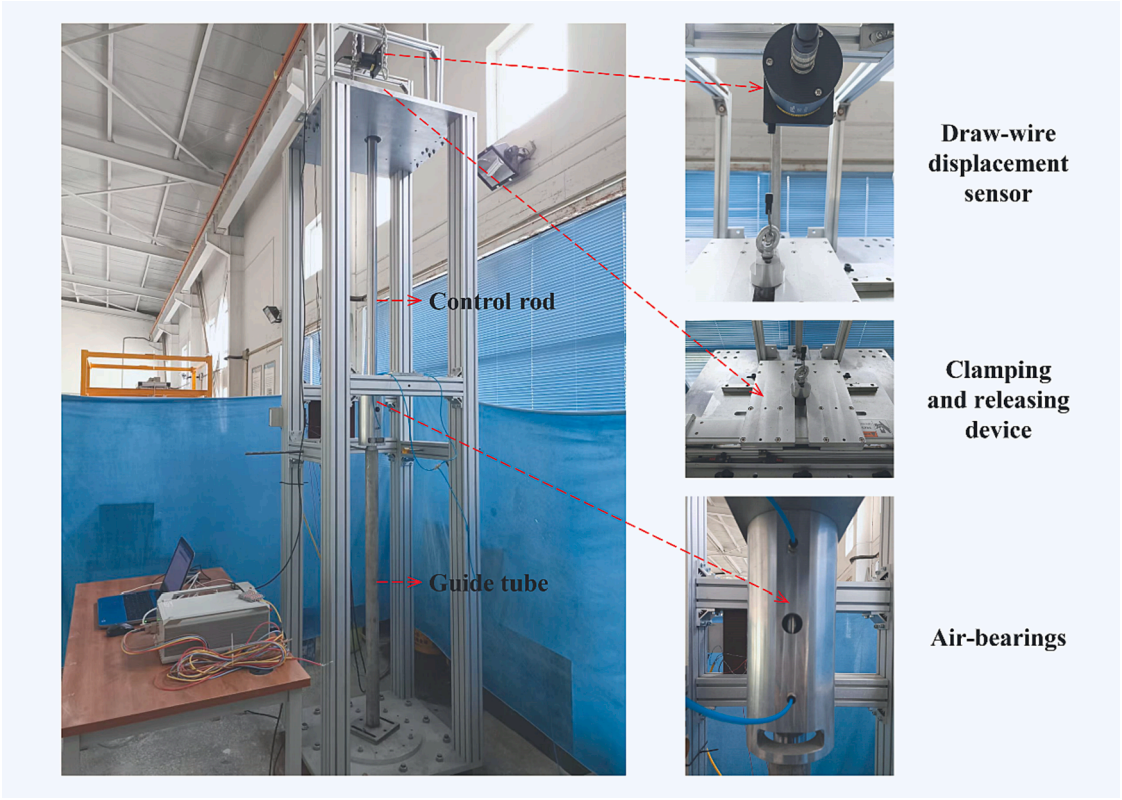


**Fig. 4.** Snapshot picture of experimental set-up.

fluid flows upward, i.e.

$$v = \frac{dy}{dt} + v_w \tag{14}$$

in which $v_w$ is the upward annular gap flow velocity of fluid.

The theoretical analysis of $v_w$ is difficult for extreme operating conditions such as large blockage ratio and large eccentricity, thus, it is needed to perform the inverse calculation by combining the CFD simulation results and the physical model experiment results. In the present study, we can first calculate an average velocity of upward flow of the fluid through flow conservation, and then divide it by a coefficient to correct it:

$$v_w = \frac{1}{\gamma} V_a \tag{15}$$

where

$$V_a = \frac{r^2}{R^2 - r^2} \frac{dy}{dt} \tag{16}$$

is the average flow velocity of the cross-section of the annular gap, and $\gamma$ is the correction coefficient for annular gap flow velocity. Here, we determine $\gamma$ via the CFD simulations and the experimental results.

(5) Pressure drag

Pressure drag is caused by the flow separation at the trailing edge of the control rod due to the existence of viscosity and the pressure at the tail to be lower than that at the head (i.e., the dynamic differential pressure), which can be calculated by the following formula (Zhou et al., 2013):

$$F_p = C_D \frac{1}{2} \rho v^2 A_{rea} \tag{17}$$

in which $C_D$ is the drag coefficient and it is related to parameters such as the Reynolds number and the length-to-diameter ratio of the control rod.

When $Re \ll 1$, $C_D$ can be calculated according to the Stokes theoretical solution under small Reynolds number flow conditions, while, for $10^3 < Re < 10^5$, $C_D$ is independent of Reynolds number and remains basically constant, i.e.

$$C_D = \begin{cases} \dfrac{64}{Re} \text{ for } Re << 1 \\ 1.2 \text{ for } 10^3 < Re < 10^5 \end{cases} \tag{18}$$

The final governing equation of eccentric rod drop can be obtained by substituting the above force components into Eq. (1):

$$mg - \rho y A_{rea} g - m\frac{d^2y}{dt^2} - f\frac{y}{D_E}\frac{1}{2}\rho\left(\frac{dy}{dt} + v_w\right)^2 A_{rea} - C_D\frac{1}{2}\rho\left(\frac{dy}{dt} + v_w\right)^2 A_{rea} = m\frac{d^2y}{dt^2} \tag{19}$$

with the initial conditions:

$$\begin{cases} \left.\dfrac{dy}{dt}\right|_{t=0} = 0 \\ \left.\dfrac{d^2y}{dt^2}\right|_{t=0} = g \end{cases} \tag{20}$$

The displacement time histories, the velocities, accelerations, and hydrodynamic characteristics of the control rod can be obtained by solving the above second-order variable coefficient nonlinear ordinary differential equation. When ground excitation and the deformation of the control rod have to be considered, the contact and friction between the control rod and the guide tube should be added to the theoretical model to meet the requirements of different control rod drop states.

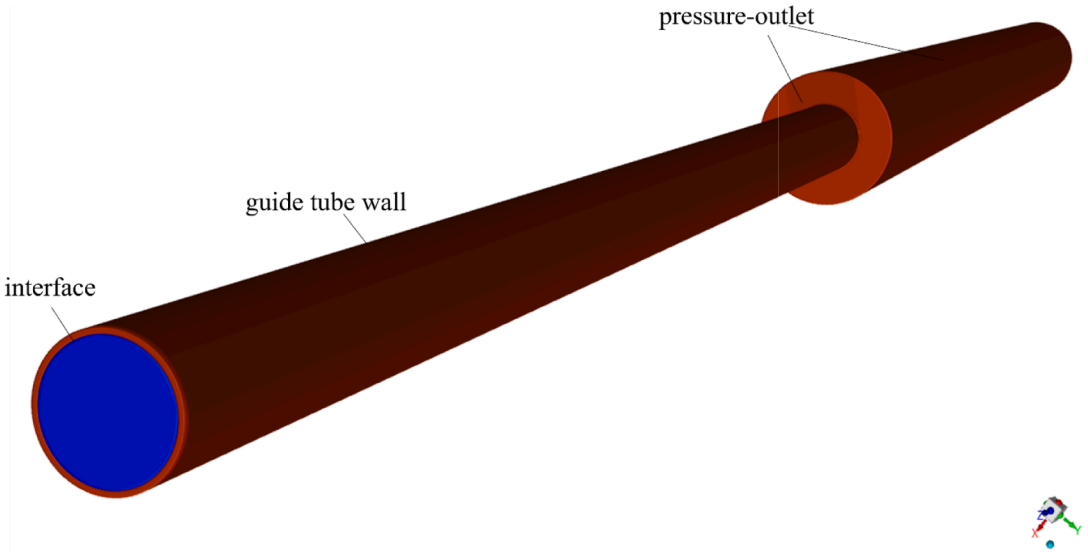


(a)

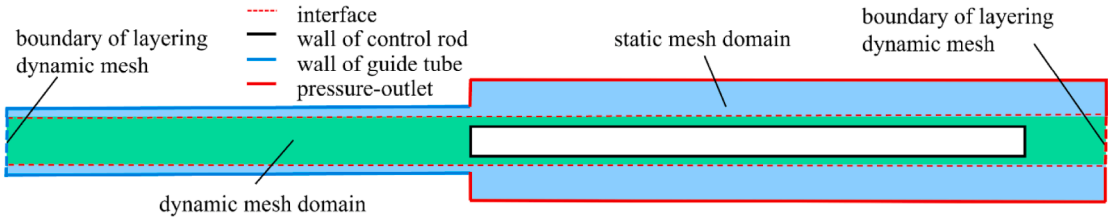


(b)

**Fig. 5.** Computational domain: (a) schematic of three-dimensional computational domain; (b) schematic of cross-section computational domain showing boundary conditions.

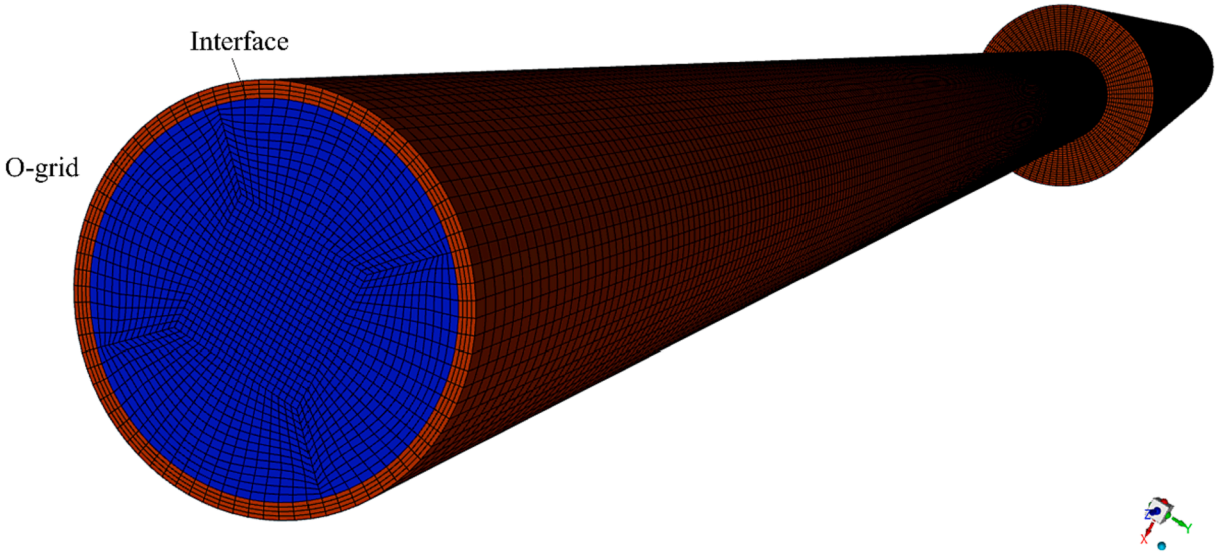


**Fig. 6.** Overall view of the computational domain with structured hexahedral grids.

### *2.3. Theoretical calculation conditions*

As shown in Table 1, the diameter of the control rod $r = 50$ mm, the blockage ratio $\alpha$ is adjusted by varying the diameter of the guide tubes. In this study, $R = 100$ mm, 75 mm, 60 mm, and 55 mm, and the corresponding blockage ratios are equal to 0.50, 0.67, 0.83, and 0.91 respectively. The eccentricity $\beta = 0$ and 1.0 in this study.

The length of the control rod $L$ is 1.60 m, and the height of the guide

**Table 2**
Models for mesh dependency check.

| Mesh | Sizes (mm) | Nodes | Meshes |
|---|---|---|---|
| M1 | 6.0 | 304,123 | 267,100 |
| M2 | 5.0 | 369,302 | 324,800 |
| M3 | 4.0 | 456,645 | 401,500 |
| M4 | 2.0 | 911,727 | 802,500 |

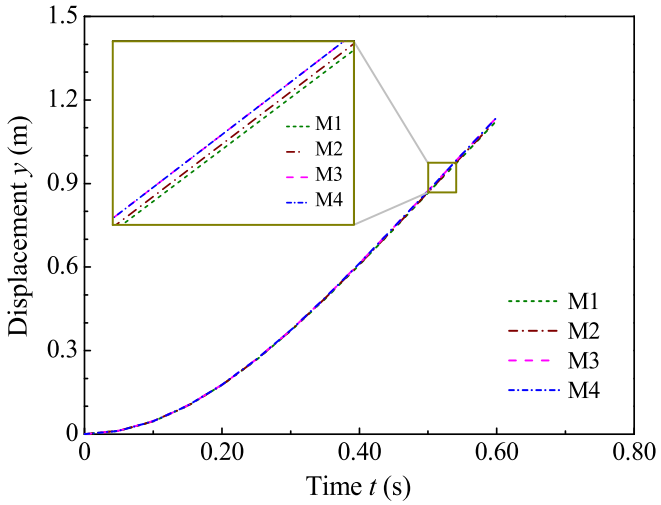


**Fig. 7.** Displacement time histories for acrylic rod with four different grid sizes: $\alpha = 0.50$, $\beta = 0$.

**Table 3**
CFD simulation conditions.

| | $\beta = 0$ | $\beta = 0.9$ |
|---|---|---|
| $\alpha = 0.50$ | Case 9 | Case 10 |
| $\alpha = 0.67$ | Case11 | Case 12 |
| $\alpha = 0.83$ | Case 13 | Case 14 |
| $\alpha = 0.91$ | Case 15 | Case 16 |

tube is 1.25 m. The guide tube was filled with water. At the initial state, the bottom of the control rod is in contact with the free surface of the water in the guide tube, so that the drop height was approximately 1.25 m.

## 3. Physical model experiment of eccentric rod drop

### 3.1. Experimental set-up

In this study, we designed an experimental device to realize the annular gap flow with adjustable eccentricity, as shown in Fig. 4. The experimental device was installed vertically on the self-leveling epoxy floor and checked with a level bar. The guide tube was rigidly connected onto the baseboard. A pair of air-bearings was installed in the middle of the device to ensure that the control rod was parallelly aligned with the guide tube, and the lateral displacement of the control rod was limited due to the small air gap (4 μm). The air-bearings also provides load-carrying capability to avoid possible physical contact between the control and the outer-sleeves of the air-bearings, so the mechanical friction force can be ignored.

The blockage ratio was adjusted by varying the diameter of the guide tube. The eccentricity between the control rod and the guide tube was adjusted by adjusting the lateral position of the guide tube through the slide at the bottom. At the top of the device, an electric clamping and releasing device was used to release the control rod. The length of the control rod $L$ is 1.60 m, the height $h$ of the guide tube is 1.28 m, and a 0.03 m thick cushion block is placed at the bottom for buffering, so that the drop height was also approximately 1.25 m.

### 3.2. Experimental methods and conditions

First, adjusting the blockage ratio and eccentricity by replacing the guide tubes with different diameter, then fill the guide tube with water, and release the control rod trough the electric clamping and releasing device. The displacement time histories of the control rod drop were recorded synchronously by a draw-wire displacement sensor (see Fig. 4) with a resolution of 0.3 mm, and the sampling rate was 1000 Hz. The errors of the experimental data should include the random errors from random factors in measurement, and the bias errors from measurement instrument accuracy, operating procedures, operating methods and etc. It should be noted that in order to ensure the reliability of experimental data, at least one repeated experiment was conducted for each experimental condition to verify the stability of the measurement results and eliminate the interference of random errors, the bias errors were minimized by the high-precision displacement sensor.

The test conditions are the same with that of theoretical calculation, i.e., blockage ratio $\alpha = 0.50$, 0.67, 0.83, and 0.91 ($r = 50$ mm, $R = 100$ mm, 75 mm, 60 mm, and 55 mm), eccentricity $\beta = 0$, 1.0. Two kinds of control rods were used in the experiment to investigate the influence of the weight of the control rod: stainless steel rod and acrylic rod, with

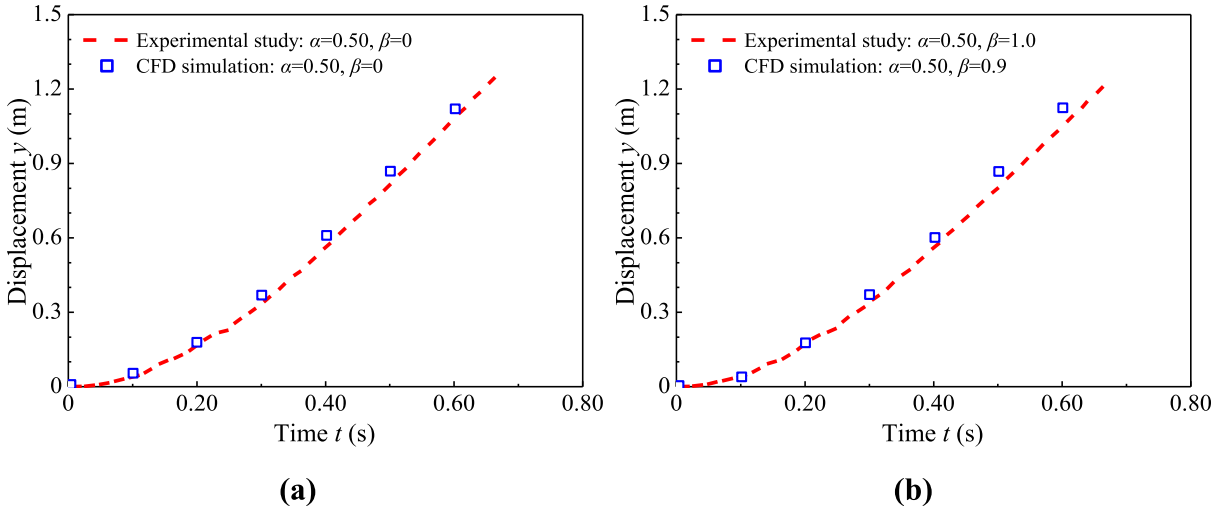


**Fig. 8.** Comparisons of displacement time history between CFD simulations and experiments for acrylic rod: (a) $\alpha = 0.50$, $\beta = 0$; (b) $\alpha = 0.50$, eccentric state.

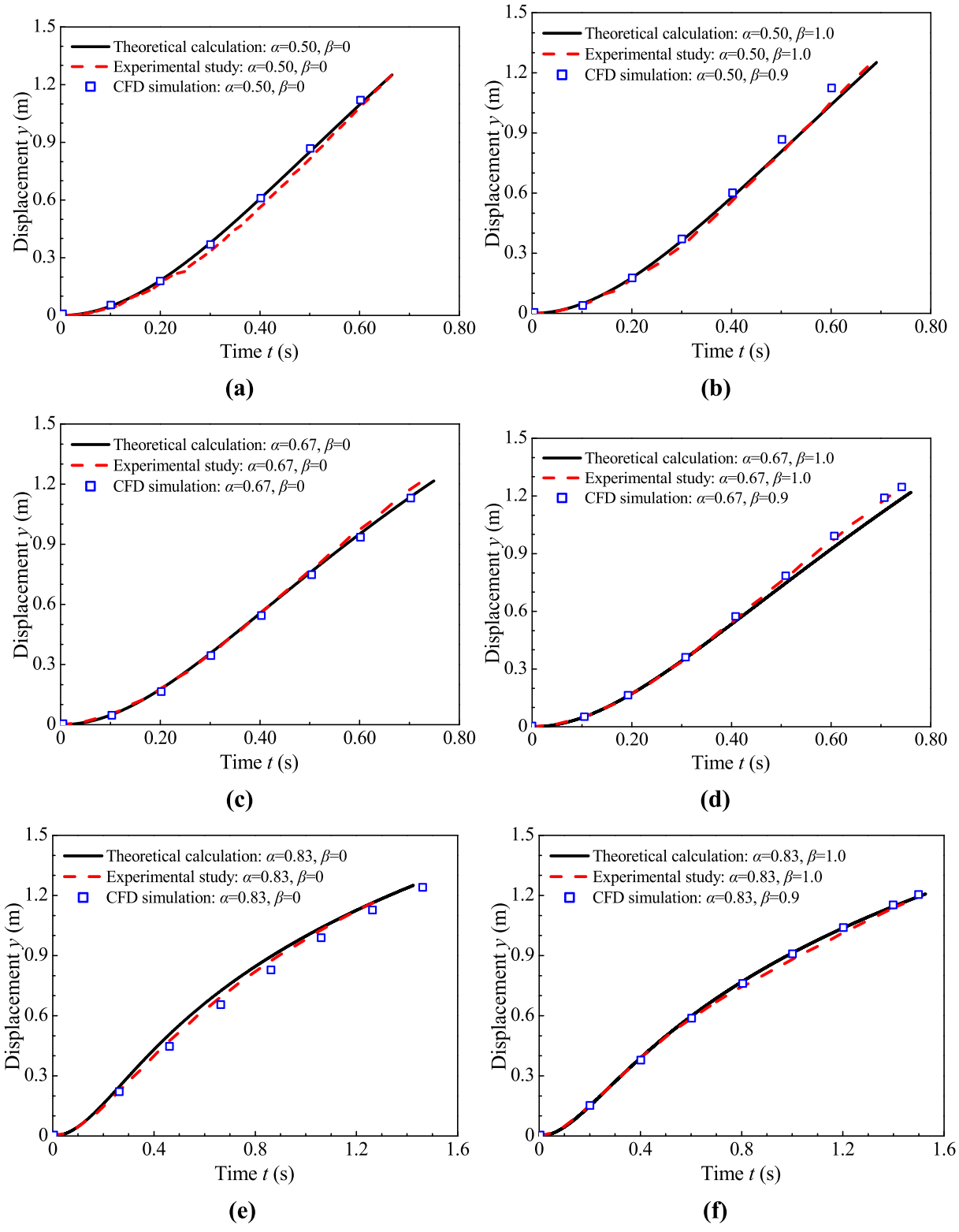


**Fig. 9.** Comparisons of displacement time history among theoretical calculations, experiments and CFD simulations for acrylic rod: (a) $\alpha = 0.50$, $\beta = 0$; (b) $\alpha = 0.50$, eccentric state; (c) $\alpha = 0.67$, $\beta = 0$; (d) $\alpha = 0.67$, eccentric state; (e) $\alpha = 0.83$, $\beta = 0$; (f) $\alpha = 0.83$, eccentric state; (g) $\alpha = 0.91$, $\beta = 0$; (h) $\alpha = 0.91$, eccentric state.

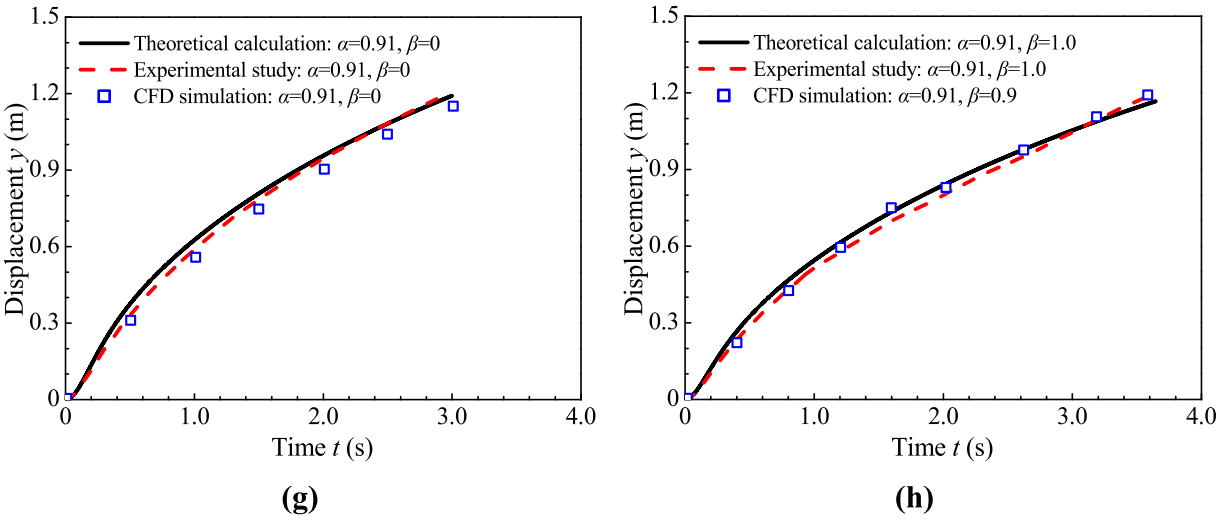


**Fig. 9.** (*continued*).

**Table 4**
Velocity correction coefficient $\gamma$ for annular gap flow.

| | $\beta = 0$ | $\beta = 1.0$ |
|---|---|---|
| $\alpha = 0.50$ | 1.0 | 1.0 |
| $\alpha = 0.67$ | 1.3 | 1.3 |
| $\alpha = 0.83$ | 1.7 | 1.3 |
| $\alpha = 0.91$ | 2.1 | 1.55 |

densities being 7800 kg/m$^3$ ($m = 24.5$ kg) and 1200 kg/m$^3$ ($m = 3.8$ kg), respectively.

## 4. CFD simulation

### 4.1. Mathematical formulations

As the problem considered in this study involves gas–liquid interfacial flow with moving boundaries, the volume of fluid (VOF) method and dynamic mesh technique are used to conduct numerical simulations with the commercial CFD software, ANSYS Fluent (ANSYS Inc., 2022).

(1) Conservation equations for fluid flow.

Incompressible, variable-density, Navier-Stokes equations with gravity and interfacial tension are given by (ANSYS Inc., 2022):

$$\nabla \cdot \boldsymbol{u} = 0 \tag{21}$$

$$\frac{\partial}{\partial t}(\rho \boldsymbol{u}) + \nabla \cdot (\rho \boldsymbol{u}\boldsymbol{u}) = -\nabla p + \nabla \cdot [\mu(\nabla \boldsymbol{u} + \nabla \boldsymbol{u}^T)] + \boldsymbol{F} \tag{22}$$

$$\partial_t \rho + \nabla \cdot (\rho \boldsymbol{u}) = 0 \tag{23}$$

in which $\rho$ represents the density of fluid, $\boldsymbol{u}$ represents the velocity vector, $\mu$ is the dynamic viscosity, $\boldsymbol{F}$ is the source term for the momentum equation. $\boldsymbol{F}$ is given by:

$$\boldsymbol{F} = \rho \boldsymbol{g} + \boldsymbol{f}_\sigma \tag{24}$$

in which $\boldsymbol{f}_\sigma$ is the surface tension force.

In this study, the two fluids, water and air, are named fluids 1 and 2, respectively. In the VOF method, a volume fraction field $c(x, t)$ is used to capture the air-water interface. The density and viscosity of the mixture obey the mixing rule:

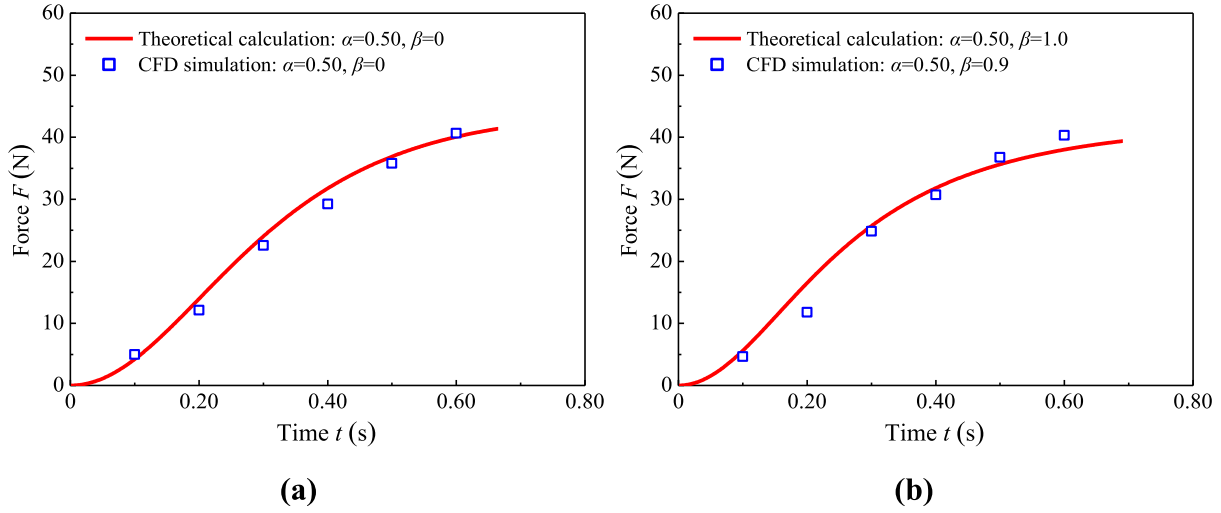


**Fig. 10.** Comparisons the hydrodynamic characteristic of control rod between theoretical calculations and CFD simulations for acrylic rod: (a) $\alpha = 0.50$, $\beta = 0$; (b) $\alpha = 0.50$, eccentric state; (c) $\alpha = 0.67$, $\beta = 0$; (d) $\alpha = 0.67$, eccentric state; (e) $\alpha = 0.83$, $\beta = 0$; (f) $\alpha = 0.83$, eccentric state; (g) $\alpha = 0.91$, $\beta = 0$; (h) $\alpha = 0.91$, eccentric state.

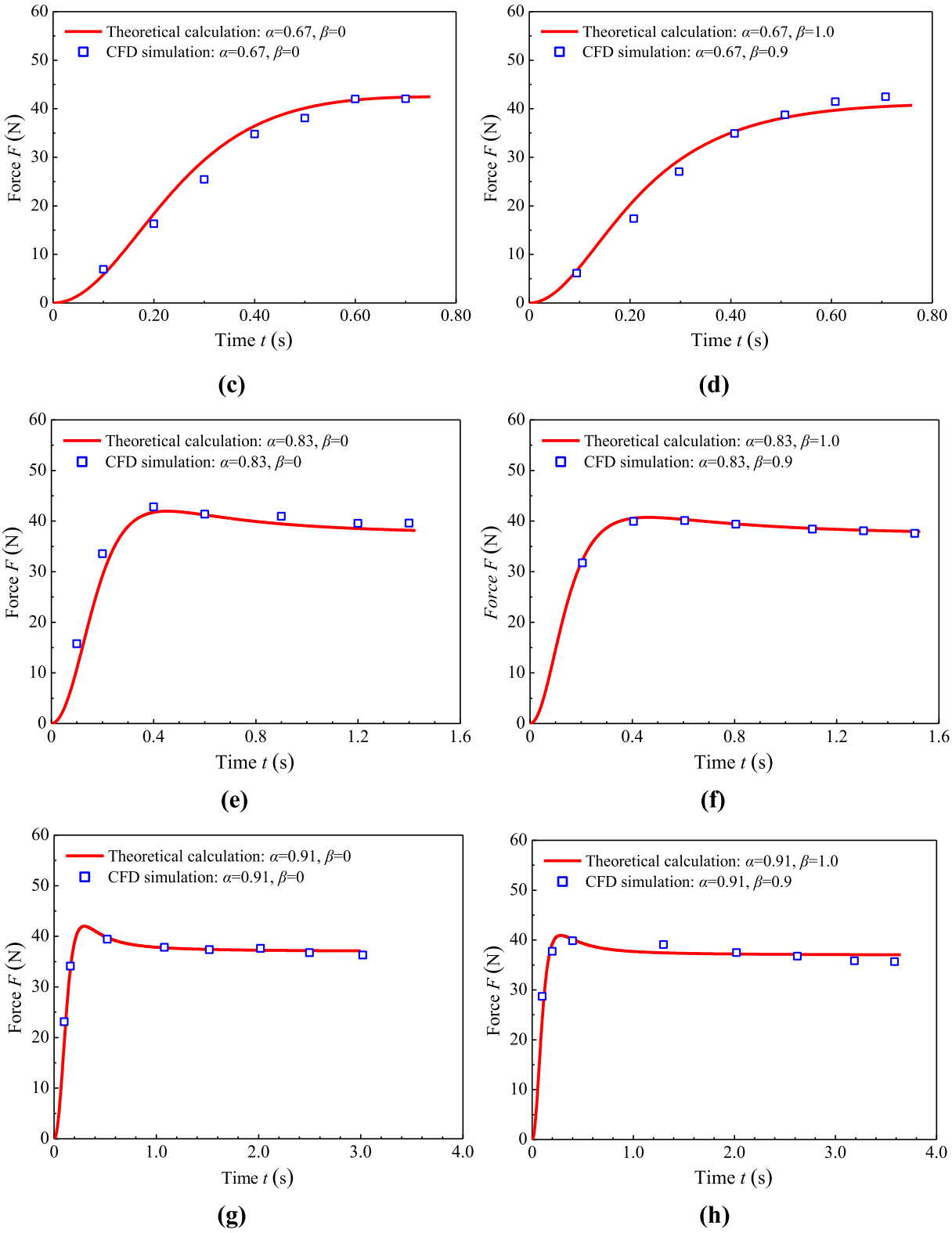


**Fig. 10.** (*continued*).

$$\rho(c) = c\rho_1 + (1-c)\rho_2 \tag{25}$$

$$\mu(c) = c\mu_1 + (1-c)\mu_2 \tag{26}$$

in which $\rho_1$, $\rho_2$ and $\mu_1$, $\mu_2$ being the densities and dynamic viscosities of water and air, respectively. $c$ represents the volume fraction of water.

Thus, Eq. (22) can then be replaced with an equivalent advection equation for $c$.

$$\partial_t c + \nabla\cdot(c\boldsymbol{u}) = 0 \tag{27}$$

(2) Dynamic mesh flow field equation.

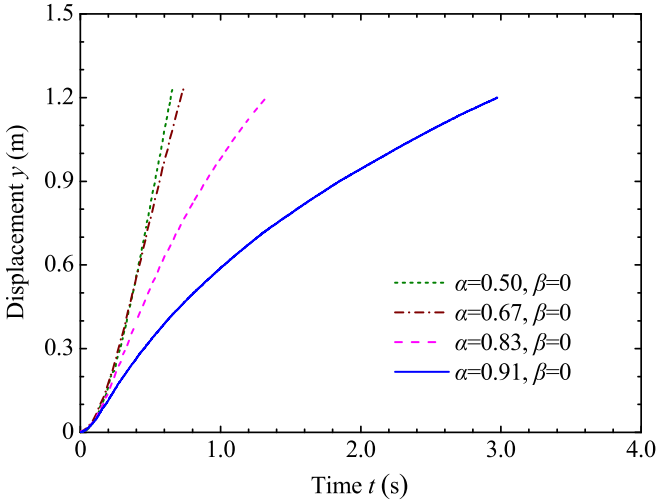


**Fig. 11.** Displacement time histories of control rod drop with different blockage ratios under center alignment state for acrylic rod.

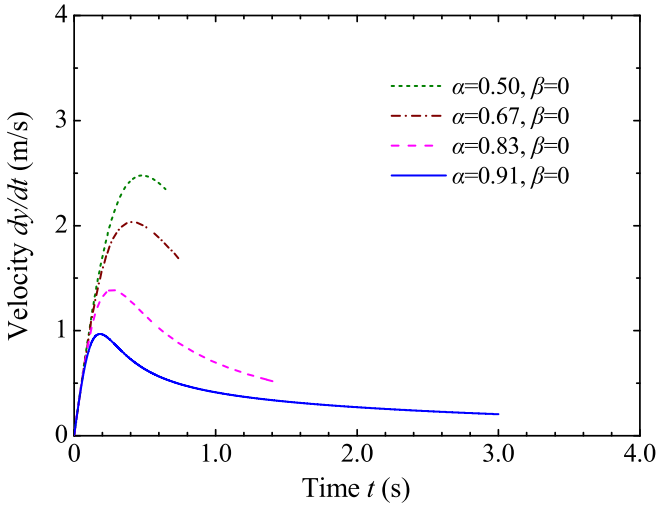


**Fig. 12.** Velocities of control rod drop with different blockage ratios under center alignment state for acrylic rod.

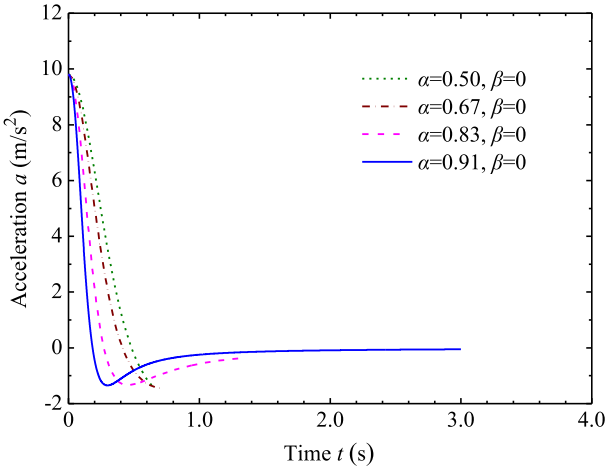


**Fig. 13.** Accelerations of control rod drop with different blockage ratios under center alignment state for acrylic rod.

Dynamic mesh technique based on layering is used to investigate the unsteady flow fields involving moving boundaries and objects, and it has been proofed to be an efficient tool in simulating the flow fields accompanied by an accelerating control rod (Rabiee and Atf, 2016; Cheng et al., 2020).

The partial differential form of the transport equation of the general scalar in the dynamic mesh can be established as follows:

$$\frac{\partial}{\partial t}(\rho\phi)+\frac{\partial}{\partial x}[\rho\phi(\boldsymbol{u}-\boldsymbol{u}g)]=\frac{\partial}{\partial x}(\Gamma\frac{\partial\phi}{\partial x})+S_{\phi} \tag{28}$$

in which $\phi$ is the general scalar quantity, $\boldsymbol{u}_g$ is the speed of grid motion, $\Gamma$ is the diffusion coefficient, $S_\phi$ is the source term of $\phi$ (ANSYS Inc., 2022).

### 4.2. Grid settings

As schematically shown in Fig. 5 in both 3D and cross-sectional views, the whole computational domain includes the geometry of the guide tube and a cylinder whose diameter is larger than the guide tube (see Fig. 5(a)). At the same time, the volume of the control rod is subtracted from the domain. The cylinder represents the space outside the guide tube, while a small diameter is used to reduce the numerical cost.

Boundaries of the guide tube and control rod are set as walls. Boundaries of the cylinder are set as pressure-outlet except for the area connected to the boundary of the guide tube.

To simulate the motion of the control rod, the whole computational domain is divided into two subdomains by a cylindrical surface with a diameter larger than the control rod and smaller than the guide tube (see Fig. 5(b)). The outer part is the static mesh domain, and the inner part is the dynamic mesh domain with the boundaries of the control rod. The information exchange between the two domains takes place through the interface.

As the motion of the control rod only along the axial direction, the dynamic mesh domain is restricted to moving only in the axial direction. During the movement of the dynamic mesh domain, only the two layers of meshes at its two ends are dynamically changed by the layering method through splitting and collapse operations to control the generation and disappearance of the mesh layers, respectively, while keeping the positions of the end boundaries of the dynamic mesh domain fixed. The default settings for mesh splitting and collapsing are 0.40 and 0.20, respectively. That is, if the size of the mesh on the moving boundary is larger than 1.40 times the original mesh size, it will be split into two new meshes. Conversely, if the size of the mesh on the moving boundary is smaller than 0.20 times the basic mesh size, two meshes will be combined.

To maintain accuracy and reduce the computational cost, ANSYS ICEM is used to generate structured hexahedral grids, as shown in Fig. 6. The computational domain is split into blocks using the O-grid method, and extra blocks are deleted to create a multi-block partition. The hexahedral meshes have larger edge lengths in the z-direction because it is much larger than the x- and y-directions, and this reduces the computational cost to a proper level. The meshes between the interface and the wall of the guide tube and the wall of the control rod are set to four layers. The mesh around the cylinder is set to 80.

### 4.3. Computational settings

The simulation is conducted under an ambient pressure of one atmosphere and a temperature of 20°C. Under those conditions, the density of water is 998 kg/m$^3$ and the dynamic viscosity of water is $1.003\times10^{-3}$ kg/(m$^2$·s), while those of air are 1.225 kg/m$^3$ and $1.7894\times10^{-5}$ kg/(m$^2$·s), respectively. The boundary condition of the outlet of the fluid domain is set as the pressure outlet, and the gauge pressure is 0 Pa. The initial speed of the control rod is set at 0 m/s. All the solid walls are set to no slip and no penetration.

The finite volume method (FVM) is used to discretize the fluid

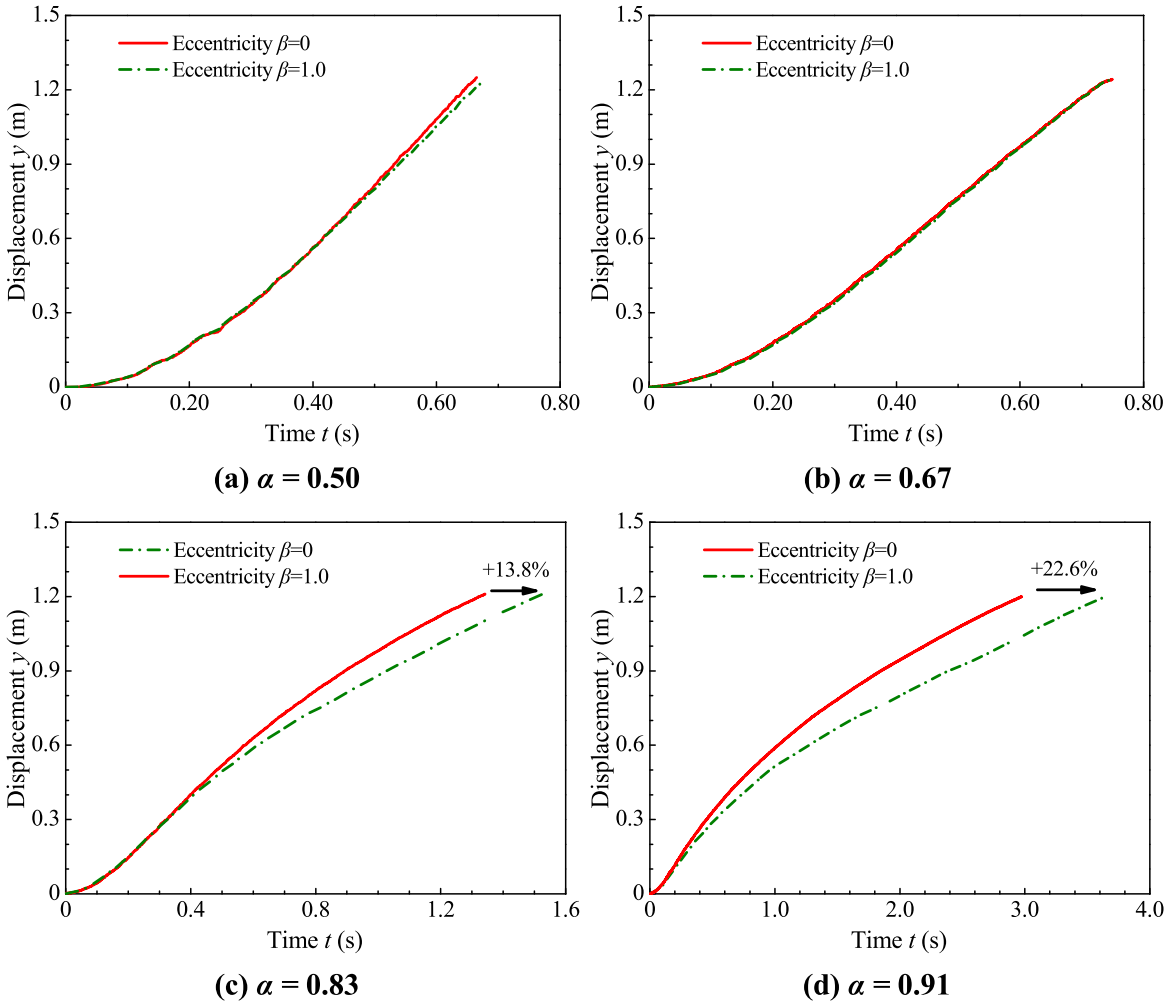


**Fig. 14.** Comparisons of displacement time history between concentrically located control rod and eccentrically ones for the acrylic rod.

computational control equations and transform the partial differential equations into algebraic equations, which are solved using the Semi-Implicit Method for Pressure Linked Equations (SIMPLE) algorithm. A two-phase flow model, which solves the flow in the air and water simultaneously is employed in the present study. As aforementioned in section 4.1, the VOF method is used to track the free surface. The standard format is selected as the pressure interpolation format. The Geo-Reconstruct method in Ansys Fluent is selected as the interpolation format of volume fraction. The second-order upwind format is selected as the interpolation format for momentum, turbulent kinetic energy, and turbulent dissipation rate.

The temporal discretization is set to be first-order. When the blockage ratios are 0.50 and 0.67, a fixed time step is used, and the time step is $1\times10^{-4}$ s. With the increase of blockage ratio, the calculation time increases. To improve the numerical efficiency, the adaptive time step method is applied for blockage ratios of 0.83 and 0.91 with the maximum Courant number is 2. The initial time step is $1\times10^{-5}$ s, while the minimum time step is $1\times10^{-6}$ s, and the maximum time step is set to $1\times10^{-4}$ s. The minimum and maximum time step change factors are 0.8 and 1.2, respectively.

### 4.4. Grid independence study

In order to analyze the grid sensitivity in this study, four grid division forms of different sizes (see Table 2) were carried out for $\alpha = 0.50$ and $\beta = 0$. It should be noted that the mesh size of the cylindrical section is unchanged, and the mesh size of the longitudinal section is changed. The displacement time histories for the acrylic rod with four different grid sizes are shown in Fig. 7. At different grid sizes, the displacement time history is consistent, and drop time deviation is less than 1 %, which indicates that the current model mesh setup of M3 is sufficiently refined for the present analyses. In this study, a grid size of 4.0 mm was selected for the next control rod drop analysis.

### 4.5. CFD simulation conditions

CFD simulations are carried out for the acrylic rod, and the simulation conditions are summarized in Table 3. Consistent with the theoretical model calculation and physical model experiment conditions, the blockage ratios were set to 0.50, 0.67, 0.83, and 0.91 ($r = 50$ mm, $R = 100$ mm, 75 mm, 60 mm, and 55 mm). However, due to the difficulties in the CFD simulations for the meshes in the small gap between the control rod and the guide tube, the eccentricities were set to 0 and 0.9. The maximum eccentricity ($\beta = 0.9$) is slightly smaller than that in theoretical model calculation and physical model experiment ($\beta = 1.0$).

## 5. Results and discussions

### 5.1. Validation of the CFD simulation

The CFD model is validated by comparing the present model predictions with the experimental measurements, as shown in Fig. 8. It should be noted that, the eccentricity $\beta$ is equal to 0.9 in the CFD simulation, whereas it is 1.0 in the experiment for eccentric state (see

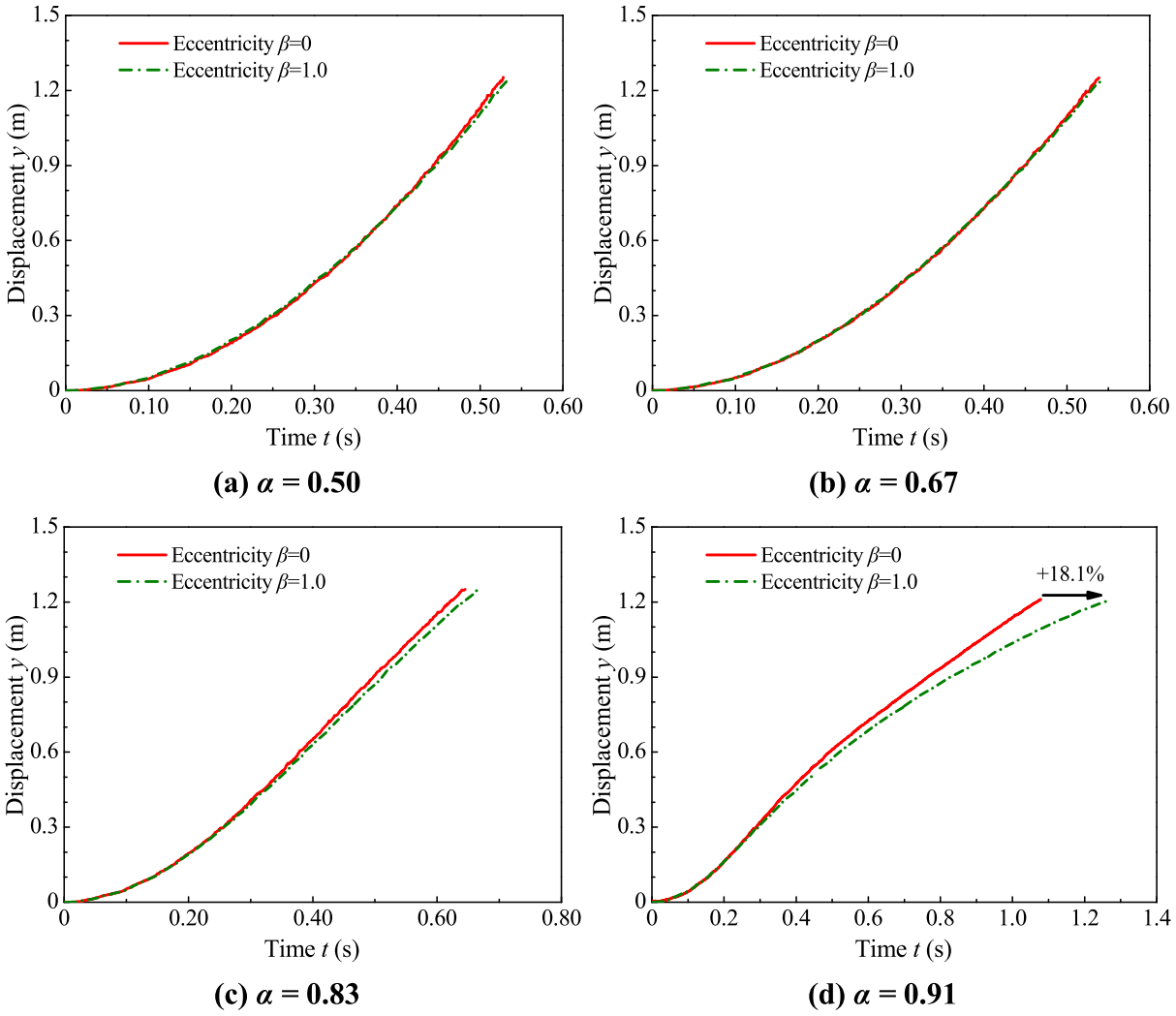


**Fig. 15.** Comparisons of displacement time history between concentrically located control rod and eccentrically ones for stainless steel rod.

Fig. 8(b)), but subsequent results show that such a small deviation between the eccentricity has little impact on control rod drop (see Fig. 9). It can be seen from Fig. 8 that the present numerical results agree well with the experiment results with respect to both center alignment state and eccentric state; the CFD model is applicable and effective for eccentric rod drop simulation. Further, we can improve the upward annular gap flow velocity $v_w$ in the theoretical model using the CFD simulation results.

### 5.2. Modification of the theoretical model

As aforementioned in section 2.2, the upward annular gap flow velocity ($v_w$) of fluid should be determined by inverse calculation according to the CFD simulation results and the physical model experiment results. The displacement time histories, the velocity, acceleration, and hydrodynamic characteristics of the control rod can be extracted from the CFD simulation results. Substituting the displacement $y$, the velocity $\frac{dy}{dt}$, and the acceleration $\frac{d^2y}{dt^2}$ into Equation (19), the upward annular gap flow velocity can be calculated according to the CFD simulation results, and the annular gap flow velocity correction coefficients ($\gamma$) for the acrylic rod are summarized in Table 4.

Fig. 9 shows the comparisons of displacement time history among theoretical calculations, physical model experiments and CFD simulations after the modification of the theoretical model for the acrylic rod. It can be seen that the displacement time histories obtained from different methods are almost identical. Thus, the present study can provide a general analysis method for eccentric drop of a control rod in the guide tube with annular gap flow. Following this method, we can obtain the drop time, velocity, acceleration, and hydrodynamic characteristic, and the eccentricity effect on control rod drop could be investigated.

Fig. 10 shows consistency of the hydrodynamic characteristic of the control rod between theoretical calculations and CFD simulations after the modification of the theoretical model for the acrylic rod. Note that, the force $F$ showing in Fig. 10 is the sum of the buoyancy, fluid inertia force, viscous friction drag, and pressure drag (see section 2.1, Eq. (1)) acting on the control rod. The gravity of the control rod is 36.9 N.

### 5.3. Effects of blockage ratio on rod drop process

Fig. 11 gives the theoretical calculation results of the displacement time histories of control rod drop with different blockage ratios under center alignment state for the acrylic rod. It can be seen that with the increase of blockage ratio, the time of dropping increases drastically, especially when the blockage ratio increases from 0.83 to 0.91. This is mainly because the viscous friction drag which is proportional to the square of the relative velocity $v$ between the control rod and the fluid flow increases significantly with the increase of blockage ratio (compare Fig. 17(a, c, e and g)).

The theoretical calculation results of velocities of control rod drop ($dy/dt$) with different blockage ratios under center alignment state for

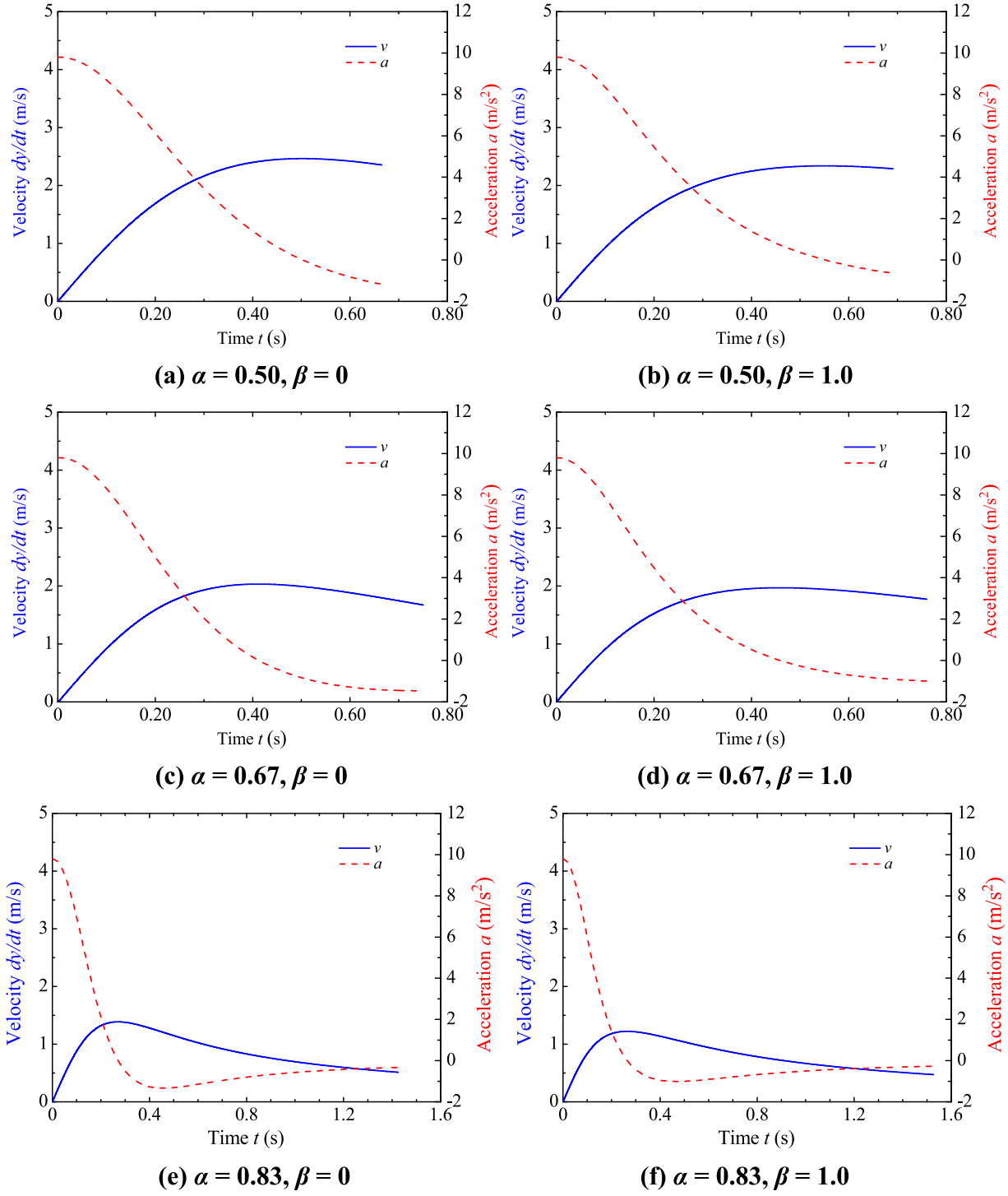


**Fig. 16.** Comparisons of velocity and acceleration between concentrically located control rod (a, c, e, g) and eccentrically located ones (b, d, f, h) for acrylic rod with different blockage ratios.

the acrylic rod are given in Fig. 12. As indicated by Fig. 12, the velocity of control rod drop increases rapidly at the initial stage under the action of gravity; thereafter with the drop the forces on the control rod reached equilibrium and the velocity reached its maximum; with the continuously dropping of the control rod, the buoyancy, viscous friction drag, and pressure drag continue to increase and upward force is greater than gravity (see Fig. 10(a, c, e and g)) and the velocity decreases. The maximum velocity of control rod drop decreases markedly with the increase of blockage ratio.

Fig. 13 shows the theoretical calculation results of accelerations of control rod drop with different blockage ratios under center alignment state for the acrylic rod. It can be seen that the acceleration decreases quickly with the dropping of the control rod, and enters into the deceleration dropping stage (i.e., the acceleration is negative) in the end for all blockage ratios. The acceleration decreases faster for greater blockage ratios. But for blockage ratio $\alpha = 0.83$ and 0.91, the acceleration gradually recovers from negative to 0, as the viscous friction drag and pressure drag decrease (see Fig. 17(e and g)) with the decrease of

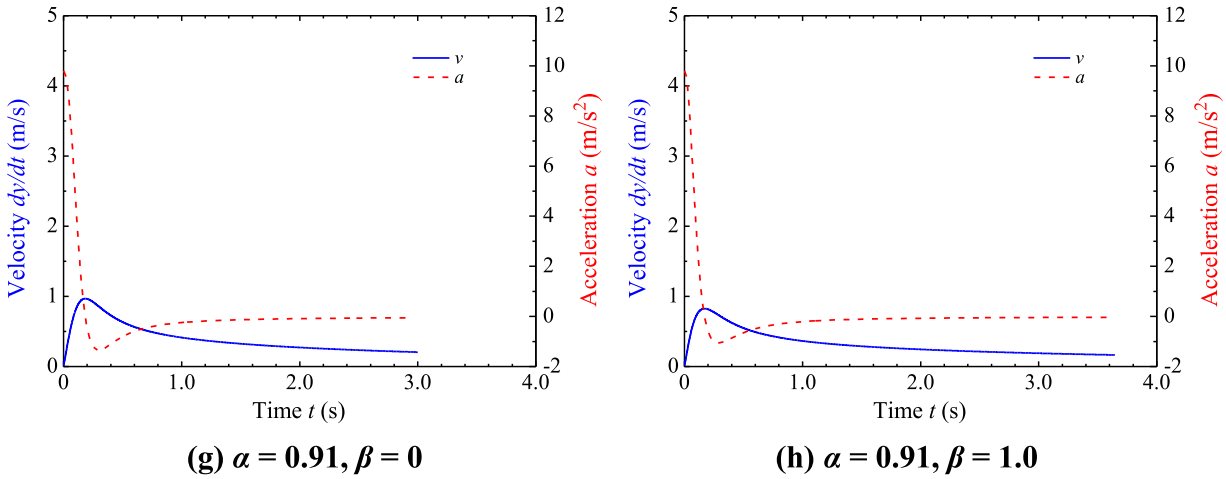


**Fig. 16.** (*continued*).

the velocity (see Fig. 12), and the forces on the control rod tends to balance (see Fig. 10(e and g)).

### 5.4. Effects of eccentricity on rod drop process

In this section, the eccentricity effect on control rod drop was evaluated. The comparisons of displacement time history between concentrically located control rod and eccentrically ones for the acrylic rod obtained from physical model experiment are presented in Fig. 14. It can be seen that, when the blockage ratio is relatively small (e.g., $\alpha < 0.83$), the eccentricity effect on drop time is negligible (see Fig. 14(a and b)), the displacement time history curve of $\beta = 1.0$ coincide with that of center alignment state ($\beta = 0$). Nevertheless, for large blockage ratio ($\alpha \geq 0.83$), the drop time increases significantly for eccentric rod drop. For $\alpha = 0.83$, the drop time for $\beta = 1.0$ increases 13.8 % than that of $\beta = 0$ (see Fig. 14(c)); and for larger blockage ratio $\alpha = 0.91$, the drop time for $\beta = 1.0$ increases 22.6 % than that of $\beta = 0$ (see Fig. 14(d)). This is mainly because the eccentricity effect will increase the upward annular gap flow velocity (see Table 4) and resulting an increase of the viscous friction drag and pressure drag (see Fig. 17).

To investigate the influence of the gravity of the control rod, we replace the acrylic rod with a stainless steel one, of which the weight are 6.5 times heavier. The comparisons of displacement time history between concentrically located control rod and eccentrically ones for stainless steel rod obtained from physical model experiment are presented in Fig. 15. The same, when the blockage ratio is relatively small (e.g., $\alpha < 0.83$), the eccentricity effect on drop time is negligible (see Fig. 15(a and b)), the displacement time history curve of $\beta = 1.0$ coincide with that of center alignment state ($\beta = 0$). Nevertheless, for large blockage ratio ($\alpha \geq 0.83$), the drop time increases significantly for eccentric rod drop (see Fig. 15(c and d)). The difference is that the eccentricity effect is slightly weaker for a heavier control rod than that of a lighter control rod. For blockage ratio $\alpha = 0.91$, the drop time for $\beta = 1.0$ increases 18.1 % than that of $\beta = 0$ (see Fig. 15(d)). This is mainly due to the gravity of the control rod which contributes to the driving force is dominant under this condition compared with the resistance force.

Fig. 16 shows the comparisons of velocity and acceleration between concentrically located control rod and the eccentrically located ones for the acrylic rod with different blockage ratios obtained from theoretical calculation. Overall, the drop velocity of eccentric state is smaller than that of concentrically located ones for all blockage ratios. For $\alpha < 0.83$ (see Fig. 16(a – d)), the increase of added mass (see Fig. 3) and corresponding fluid inertia force (see Fig. 17(a – d)) is the main cause, and this effect is relatively weak due to the fluid inertia force is beneficial for dropping during the deceleration stage; moreover, for $\alpha \geq 0.83$ (see Fig. 16(e – h)), the increase of upward annular gap flow velocity (see Table 4) resulting in an increase of corresponding viscous friction drag and pressure drag (see Fig. 17(e – h)) is the main cause, and this effect is relatively significant.

### 5.5. Hydrodynamic characteristics

Fig. 17 gives the comparisons of the forces acting on the control rod between the concentrically located control rod and the eccentrically located ones for the acrylic rod with different blockage ratios obtained from theoretical calculation. As aforementioned in section 5.4, for $\alpha < 0.83$ (see Fig. 17(a – d)), the increase of added mass will result in increased fluid inertia force for eccentric rod drop; and for $\alpha \geq 0.83$ (see Fig. 17(e – h)), the viscous friction drag and pressure drag will increase due to the increase of upward annular gap flow velocity for eccentric rod drop.

## 6. Conclusions

In this study, we proposed a theoretical model for computing the drop time of eccentric rod by considering added mass and the annular gap flow of fluid. To correct the upward annular gap flow velocity in the proposed model, we performed full-scale computational fluid simulations by using dynamic mesh technique. For validation, we designed an experimental device to realize the annular gap flow. With the help of above analysis method, we investigated analytically the eccentricity effect on the control rod drop time, velocity, acceleration, and the hydrodynamic characteristics. Conclusions are listed as follows.

1. The upward annular gap flow velocity correction coefficients in the proposed theoretical model were obtained from full-scale CFD simulations with respect to various values of the blockage ratio and the eccentricity. Thus, the present study provides a general method for eccentric rod drop analysis.
2. The drop time increases drastically with the increase of blockage ratio for the concentrically located control rod, especially when the blockage ratio increases from 0.83 to 0.91.
3. When the blockage ratio is relatively small (e.g., $\alpha < 0.83$), the eccentricity effect on drop time is negligible. Nevertheless, for large blockage ratio ($\alpha \geq 0.83$), the drop time increases significantly for eccentric rod drop, especially for a lighter control rod.
4. The direction of the inertial force of the fluid is opposite to the direction of the control rod's acceleration. Thus, the fluid inertia force prevents the control rod drop during the acceleration stage, while it is beneficial for dropping during the deceleration stage.

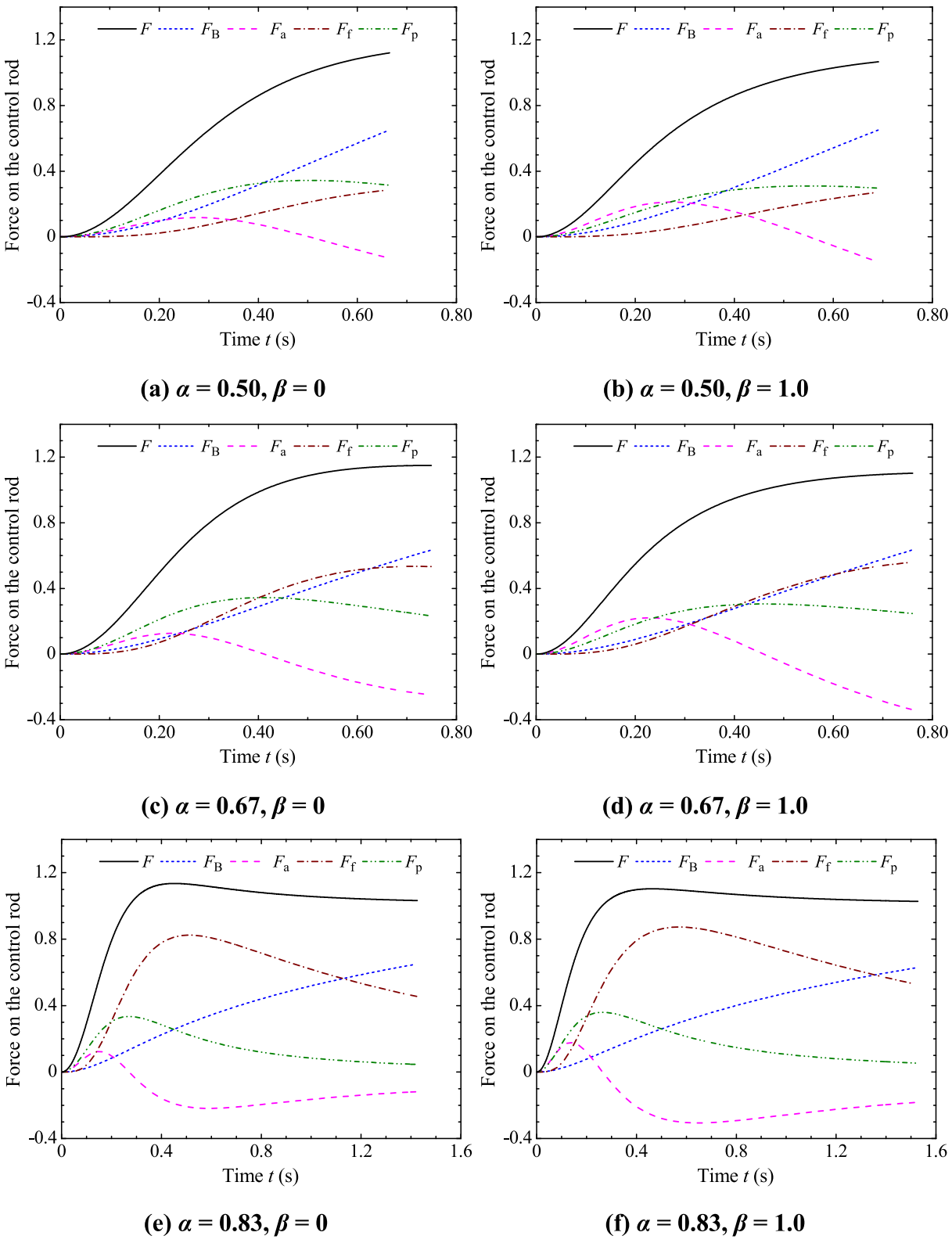


**Fig. 17.** Comparisons of forces acting on control rod between concentrically located control rod (a, c, e, g) and eccentrically located ones (b, d, f, h) for acrylic rod with different blockage ratios.

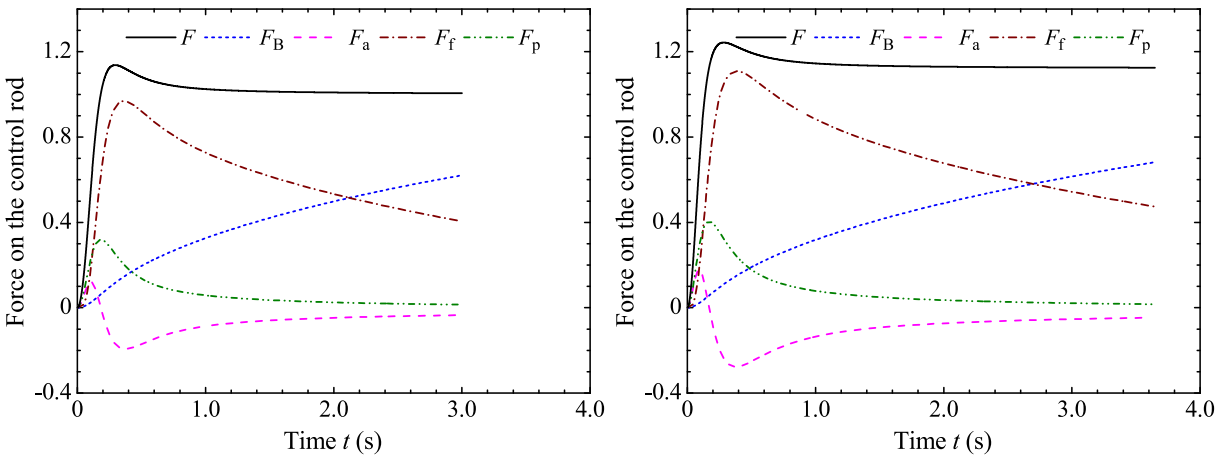


(g) $\alpha = 0.91, \beta = 0$ (h) $\alpha = 0.91, \beta = 1.0$

**Fig. 17.** (*continued*).

## Declaration of Competing Interest

The authors declare that they have no known competing financial interests or personal relationships that could have appeared to influence the work reported in this paper.

## Data availability

No data was used for the research described in the article.

## Acknowledgements

This work was financially supported by the National Natural Science Foundation of China (Grant Nos. 12022210; 12032001), by the Youth Innovation Promotion Association CAS (2018022). Instructive discussions with Professor Bo Yin and the technical supports from Mr. Fu-Lin Zhang are greatly appreciated.

## References

Andriambololona, H., Bosselut, D., Massin, P., 2007. Methodology for a numerical simulation of an insertion or a drop of the rod cluster control assembly in a PWR. Nucl. Eng. Des. 237 (6), 600–606.
ANSYS Inc.,, 2022. Ansys Fluent Theory Guide. Canonsburg, PA.
Arthur, E.M., Zhang, C.D., Debrah, S.K., Yamoah, S., Wang, L., 2020. Analysis of the drop dynamics of control rod assembly in a LBE-cooled research reactor. Ann. Nucl. Energy 149, 107778.
Bo, H.L., Zheng, W.X., Dong, D., 2000. Studies on the performance of the hydraulic control rod drive for the NHR-200. Nucl. Eng. Des. 195 (1), 117–121.
Bo, H.L., Zheng, Y.H., Zheng, W.X., Dong, D., 2002. Study on step-up characteristic of hydraulic control rod driving system. Nucl. Eng. Des. 216, 69–75.
Chen, S.S., 1975. Vibration of nuclear fuel bundles. Nucl. Eng. Des. 35, 399–422.
Cheng, J., Wang, Z.Y., Lu, C., Zhang, J.B., Bi, S.M., Feng, Q., 2020. Control rod drop hydrodynamic analysis based on numerical simulation. Front Energy Res. 8, 601067.
Chung, H., Chen, S.S., 1977. Vibration of a group of circular cylinders in a confined fluid. J Appl Mech-T ASME 44 (2), 213–217.
Donis, J.M., Goller, H., 1972. A mathematical model of a control rod drop. Nucl. Eng. Des. 23, 107–120.
Gibert, R.J., 1988. Vibrations des structures. interactions avec les fluides, sources d'excitation aléatoires. Eyrolles, Paris.
Huang, H., Wang, Z.W., Xu, W., Liu, T., Yang, Y.R., Li, P., 2018. Seismic analysis of PWR control rod drop with the CRDAC scram performance code. Ann. Nucl. Energy. 114, 624–633.
Kim, J.B., Jeong, J.Y., Lee, T.H., Kim, S., Euh, D.J., Joo, H.K., 2016. On the safety and performance demonstration tests of prototype Gen-IV sodium-cooled fast reactor and validation and verification of computational codes. Nucl. Eng. Technol. 48 (5), 1083–1095.
Lee, Y.K., Lee, J.H., Kim, H.W., Kim, S.K., Kim, J.B., 2017. Drop performance test of conceptually designed control rod assembly for prototype generation IV sodium-cooled fast reactor. Nucl. Eng. Technol. 49, 855–864.
Lin, Z.K., Zhai, L.F., Zhu, L., Wang, X., Zhang, X.C., Cao, Y., Wang, N.X., 2017. Control rod drop dynamic analysis in the TMSR – SF1 based on numerical simulation and experiment. Nucl. Eng. Des. 322, 131–137.
Mateescu, D., Païdoussis, M.P., Sim, W.G., 1994. Spectral solutions for unsteady annular flows between eccentric cylinders induced by transverse oscillations. J Sound Vib. 177 (5), 635–649.
Rabiee, A., Atf, A., 2016. Control rod drop hydrodynamic analysis for a pressurized water reactor. Progress in Nuclear Energy 88, 191–197.
Rajan Babu, V., Veerasamy, R., Patri, S., Raj, S.I.S., Krovvidi, S.K., Dash, S.K., Meikandamurthy, C., Rajan, K.K., Puthiyavinayagam, P., Chellapandi, P., Vaidyanathan, G., Chetal, S.C., 2010. Testing and qualification of Control & Safety Rod and its drive mechanism of Fast Breeder Reactor. Nucl. Eng. Des. 240 (7), 1728–1738.
Rajan Babu, V., Thanigaiyarasu, G., Chellapandi, P., 2014. Mathematical modelling of performance of safety rod and its drive mechanism in sodium cooled fast reactor during scram action. Nucl. Eng. Des. 278 (278), 601–617.
Singh, N.K., Badodkar, D.N., Singh, M., 2014. Numerical and experimental study of hydraulic dashpot used in the shut-off rod drive mechanism of a nuclear reactor. Nucl. Eng. Des. 273, 469–482.
Son, J.G., Lee, J.H., Kim, H.W., Kim, S.K., Kim, J.B., 2019. Influence of design modification of control rod assembly for Prototype Generation IV Sodium-cooled Fast Reactor on drop performance. Nucl. Eng. Technol. 51 (3), 922–929.
Taliyan, S.S., Roy, D.P., Grover, R.B., Singh, M., Govindarajan, G., 1994. Dynamics of shut-off rod drop in a PHWR. Nucl. Eng. Des. 147 (3), 311–319.
Wang, S.K., Chen, Y.N., Chyou, Y.P., Yang, T.T., 2003. Identification of damping mechanism of TRR-II reactor control rod during free fall insertion. Nucl. Eng. Des. 226 (3), 243–254.
Wang, S.Z., Wang, D., Lin, Z.H., 1994. A study of the two-phase frictional pressure drop in vertical annual channels. Journal of xi'an Jiaotong University. 28 (5), 101–109.
Yoon, K.H., Kim, J.K., Lee, K.H., Lee, Y.H., Kim, H.K., 2009. Control rod drop analysis by finite element method using fluid-structure interaction for a pressurized water reactor power plant. Nucl. Eng. Des. 239 (10), 1857–1861.
Yu, J.H., Wang, Y.T., Sun, L., Li, X.H., 2001. Calculation of the resistance of the control rod assembly when it falls in the fluid environment. Nucl. Power Eng. 22 (3), 236–241.
Zhao, K., Xu, X.M., Chen, C.Y., Wu, F., Huang, D.W., Xi, Y.Y., Zhong, W.X., 2022. Nonlinear state equation and adaptive symplectic algorithm for the control rod drop. Ann. Nucl. Energy. 179, 109402.
Zhou, X.J., Mao, F., Min, P., Lin, S.X., 2013. Calculation of drop course of control rod assembly in PWR. Atomic Energy Sci. Technol. 47 (9), 1584–1589.